0191-8141(94)00082-4

Viscous-plastic finite-element models of fault-bend folds

S. GREGG ERICKSON and WILLIAM R. JAMISON

Centre for Earth Resources Research, Department of Earth Sciences, Memorial University of Newfoundland,
St. John's, Newfoundland, Canada A1B 3X5

Abstract—In finite-element models of fault-bend folds, viscous and plastic material properties are used to simulate pressure solution creep and cataclasis, respectively. Plastic deformation occurs primarily above ramp hinges. However, a band of high plastic strain is created in the lower hanging wall as material moves over the ramp hinges. Viscous deformation dominates above the ramp and flats, where plastic deformation is negligible. Hanging-wall material undergoes layer-parallel shortening on the lower flat and lower part of the ramp, layer-parallel extension on the upper part of the ramp and upper flat, and layer-parallel shortening farther along the upper flat. The stress invariant $\sqrt{J_2'}$ is highest above the ramp hinges and below the ramp, whereas stress invariant J_1 is highest above and below the ramp. The high J_1 below the ramp suppresses plastic deformation, so that footwall deformation is predominantly viscous. In multilayer models, strain is concentrated in the weak layers, especially on the limbs of the hanging-wall anticline. In models with bedding-parallel slip surfaces in the hanging wall, the strain on fold limbs is accommodated by interlayer slip, and layers between slip surfaces develop individual neutral surfaces. The models indicate that the relative and absolute amounts of deformation in fault-bend folds resulting from pressure solution creep and cataclasis vary as a function of structural position and history.

INTRODUCTION

The nature and history of rock deformation during movement over thrust-fault ramps (Fig. 1) have been investigated using mechanical and kinematic models (e.g. Berger & Johnson 1980, Suppe 1983) as well as field observations (e.g. Wiltschko *et al.* 1985, Kilsdonk & Wiltschko 1988). Because existing models commonly use either no material properties or simple material properties, it is difficult or inappropriate to compare the results of these models directly with natural rock deformation. In an attempt to link more closely model results and field observations, the finite-element models presented here use material properties chosen specifically
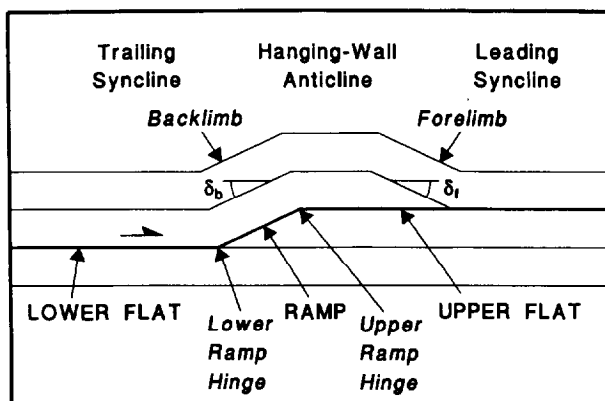

Fig. 1. Schematic drawing of a fault-bend fold, showing the terminology used in this paper (after McClay 1992). In this paper, the terms ramp, ramp hinge and flat refer to footwall ramp, ramp hinge and flat. δ_f and δ_b are the forelimb and backlimb dips.

to simulate the deformation mechanisms in low-temperature sedimentary rocks.

Kinematic models of fault-bend folding (Sanderson 1982, Suppe 1983, Johnson & Berger 1989) assume flexural-slip or flexural-flow folding during movement over a rigid footwall in order to simulate the development of a hanging-wall anticline (Rich 1934). Because layer thickness is constant in most of these kinematic models, there is layer-parallel slip or layer-parallel shear strain but no layer-parallel shortening or extension. Analytical and numerical models also have been used to simulate deformation at a ramp. Berger & Johnson (1980) model ramp anticline development above a rigid footwall using a linear viscous material, with constant friction along the ramp and frictionless flats. They show that fault friction leads to thickening of the hanging wall above the lower ramp hinge and an increase in fold asymmetry. Wiltschko (1979, 1981) uses a linear viscous, anisotropic material and a rigid, smooth footwall ramp, and assumed neutral-surface bending of the hanging wall. As material in the lower hanging wall moves over the ramp of this model, it is horizontally extended, then shortened and then extended again. Kilsdonk & Fletcher (1989) include a deformable footwall in a model of linear viscous half-spaces separated by a frictionless surface with a ramp-flat geometry, a model that produces horizontal shortening in the hanging wall at the lower ramp hinge and horizontal extension at the upper ramp hinge. In this model, the ramp maintains its initial shape but translates toward the foreland. Using an elastic-perfectly plastic finite-element model with a deformable footwall, Apperson & Goff (1991) and

Apperson (1993) find that the flattening and foreland-ward translation of a ramp and the associated deformation beneath the ramp are functions of initial ramp angle and material strength.

Low-temperature sedimentary rocks deform at the microscale and mesoscale by fracture, faulting, bedding-plane slip, pressure solution and intracrystalline plasticity (e.g. Groshong 1988). Observations of deformation adjacent to natural ramps indicate a significant contribution by all of these processes to hanging-wall deformation. Wiltschko et al. (1985) determine the timing of deformation mechanisms in the ramp region of the Pine Mountain thrust sheet of Tennessee to be layer-parallel shortening by pressure solution and twinning of calcite, followed by transport-perpendicular extension fractures, bedding-plane slip, and slip on mesoscopic faults. Kilsdonk & Wiltschko (1988) differentiate strain associated with layer-parallel shortening (twinning of calcite, transport-parallel extension fractures, transport-perpendicular stylolites and thrust faults) and later strain associated with bending (twinning of fracture fill, transport-perpendicular extension fractures, and normal faults). In addition to the hanging-wall deformation at ramps, there is also significant footwall deformation before and during thrust-fault motion (Fischer & Coward 1982, Protzman & Mitra 1990, Evans & Neves 1992) by brittle and plastic mechanisms.

The constitutive laws of a linear viscous fluid approximate those of a rock deforming by pressure solution creep (Rutter 1976), whereas pressure-dependant plasticity best characterizes deformation by fracture and cataclasis (Rudnicki & Rice 1975, Fletcher 1987). In the models presented below, we use viscous and pressure-dependant plastic material properties to model pressure solution creep and cataclasis, respectively. Although twinning and dislocation motion are important in some upper-crustal rocks, we have not included material properties to model these deformation mechanisms. Some of the models also incorporate mechanical layering and interlayer slip, both of which are important in the deformation of sedimentary sequences at upper-crustal conditions. These models simulate evolving fold geometry, as well as the sequence of deformation mechanisms during movement over a ramp, which can be compared with natural deformation.

FINITE-ELEMENT MODELS

The finite-element models presented here use a large-displacement, finite-strain Eulerian formulation and material properties that include both an elastic-plastic component and a viscous creep component. The plastic component is governed by a Drucker–Prager yield criterion (Drucker & Prager 1952)

$$F = \alpha J_1 + \sqrt{J_2'}, \qquad (1)$$

with an associated flow rule. α is a coefficient of pressure dependence, J_1 is the first invariant of stress,

$$J_1 = \sigma_{ii}, \qquad (2)$$

and J_2' is the second invariant of deviatoric stress

$$J_2' = 1/2\sigma_{ij}'\sigma_{ij}', \qquad (3)$$

where

$$\sigma_{ij}' = \sigma_{ij} - \delta_{ij}\sigma_{ii}/3, \qquad (4)$$

and

$$\delta_{ij} = 1 \text{ if } i = j, \ \delta_{ij} = 0 \text{ if } i \neq j. \qquad (5)$$

As a measure of the plastic deformation, we use equivalent plastic strain $\bar{\varepsilon}^P$ (Hill 1950), which, after n increments, is

$$\bar{\varepsilon}^P = \sum_{k=1}^{n} d\bar{\varepsilon}_k^P, \qquad (6)$$

where

$$d\bar{\varepsilon}_k^P = [(2/3) d\varepsilon_{ij}^P d\varepsilon_{ij}^P]_k^{1/2}. \qquad (7)$$

Viscous strain is described by a linear relation between stress and deformation rate,

$$\dot{\varepsilon}_{ij}^v = \sigma_{ij}'/2\eta, \qquad (8)$$

where $\dot{\varepsilon}_{ij}^v$ is the viscous deformation rate and η is the coefficient of viscosity. An equivalent viscous strain $\bar{\varepsilon}^v$ can be defined that is analogous to equivalent plastic strain. Both $\bar{\varepsilon}^P$ and $\bar{\varepsilon}^v$ are monotonically increasing internal state variables. Note that the plastic component of strain depends on J_1 but the viscous component does not. Also, the viscous component of strain is active for any non-zero value of σ_{ij}', but plastic strain occurs only if the yield criterion (equation 1) is attained.

Each model contains 462 isoparametric, quadratic elements, which are initially either 100 m × 200 m or 200 m × 200 m (Fig. 2). Plane strain is assumed. The fault surface is composed of friction-contact spring elements, and the initial fault geometry consists of a ramp connecting lower and upper flats. The ramp is 500 m high and 1000 m long, producing a ramp angle of 26.5°, and the upper and lower hinges of the ramp are rounded. A surface pressure of 75 MPa is applied to the top of the model and the right side of the hanging wall, which simulates a 3 km overburden. There is zero shear stress along this top surface of the model. A zero displacement boundary condition, $u_x = u_y = 0$, is used along the left (hinterland) side of the footwall, $u_y = 0$ along the base of the model and $u_x = 0$ along the right (foreland) side of the footwall. A displacement of 25 m per 2500 y time step is imposed on the left side of the hanging wall, a velocity (1 cm y^{-1}) that is consistent with estimates of natural thrust sheet motion (Wiltschko & Dorr 1983). The models are run to a maximum displacement of the left side of the model of 2.5 km (100 time steps). In most models, the friction coefficient along the fault is $\mu_F = 0.01$. Low friction coefficients along the fault are necessary, for the ramp angle used, to minimize internal deformation relative to fault slip. Five sets of material properties are used to simulate strong, moderate, and
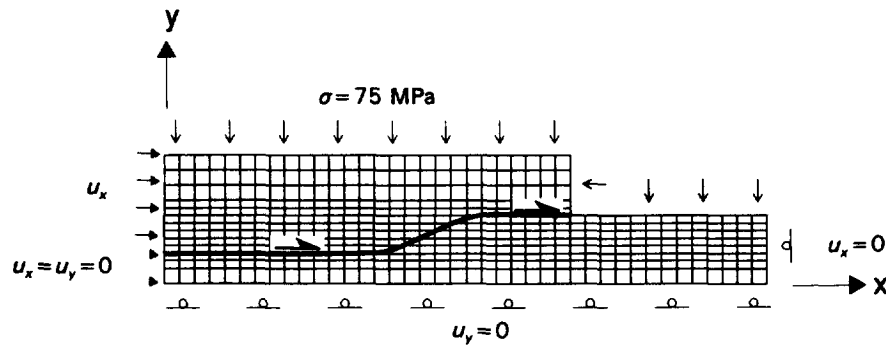
Fig. 2. Initial, undeformed grid for the finite-element model, showing boundary conditions.

Table 1. Material properties used in the models. Numbers in the fourth column are stress–strain slopes for values of stress above that in the third column, defining a piecewise linear curve

Material	Description	Yield strength (MPa)	Stress–strain slope (MPa)	Viscosity coefficient η ($\times 10^{21}$ Pa · s)
I	Strong	27	2300	5.0
	Viscous-plastic	29	350	
		31	60	
II	Moderate	27	2300	2.9
	Viscous-plastic	29	350	
		31	60	
III	Weak	10	2300	1.5
	Viscous-plastic	12	350	
		14	60	
IV	Plastic	27	2300	—
		29	350	
		31	60	
V	Weak viscous	—	—	1.5

Table 2. Model descriptions and material properties (see Table 1 for material descriptions). The forelimb and backlimb dips, δ_f and δ_b are the maximum dips after 2.5 km displacement, measured at the stratigraphic horizon that is initially midway up the ramp

Model	Description	Material	δ_f	δ_b
A	Uniform viscous-plastic	II	32°	21°
B	Uniform plastic	IV	32°	19°
C	Uniform viscous	V	39°	24°
D	Uniform viscous-plastic with rigid footwall	II	30°	22°
E	Two-layer; strong lower hanging wall and footwall, weak upper hanging wall; frictionless fault	I/III	29°	23°
F	Two-layer; strong lower hanging wall and footwall, weak upper hanging wall; frictional fault	I/III	38°	22°
G	Multilayer; six layers, alternating weak and strong	I/III	31°	22°
H	Interlayer slip along three surfaces in hanging wall	II	29°	26°

weak viscous-plastic materials, as well as viscous and plastic materials (Table 1). All materials have density ρ = 2500 kg m^{-3}, Young's modulus E = 3 × 10^4 MPa, Poisson's ratio ν = 0.25 and pressure-dependence coefficient α = 0.2 (equivalent to an internal friction coefficient of 0.28). Material properties were chosen that produce a realistic deformed geometry (minimal separation and deformation of the fault surface). These properties are generally consistent with experimentally determined properties of carbonate rocks (e.g. Johnson

1971, Turcotte & Schubert 1982). However, because strength decreases with increasing sample size (Jaeger & Cook 1971, Paterson 1978), the yield strengths used in the models are less than those determined from experimental deformation of small samples. In our models, the relationship between stress and plastic strain is piecewise linear, and hardening of the yield surface is isotropic. The plastic yield surface undergoes a minor amount of strain hardening, consistent with experimental deformation. The eight models presented here (Table 2)

investigate the effects of viscous vs plastic deformation, shallowing of the ramp by footwall deformation, friction on the fault, mechanical layering, and interlayer slip in the hanging wall.

RESULTS

Partitioning of viscous and plastic strain

Model A (Table 2) contains a hanging wall and footwall with uniform viscous-plastic material properties. Throughout most of the model evolution, $\sqrt{J_2'}$ is highest above the ramp hinges, although the maximum above the lower ramp hinges moves up the ramp during the late stages of the model (Fig. 3a). Maxima in $\sqrt{J_2'}$ also develop below the ramp and in the upper forelimb of the hanging-wall anticline. J_1 is highest immediately above and below the ramp (Fig. 3b). Incremental plastic strain occurs above the ramp hinges (Fig. 4a). As a consequence of movement of the hanging wall over the ramp hinges, a relatively uniform band of high equivalent plastic strain is created, which extends from 200–800 m above the fault. Equivalent viscous strain is highest in the backlimb and lower hinge of the hanging-wall anticline and beneath the ramp (Fig. 4b). Layer-parallel shortening develops in the backlimb and hinge of the hanging-wall anticline and in the inner arcs of the leading and trailing synclines. Layer-parallel extension develops in the outer arcs of both the hanging-wall anticline and the leading syncline. The hanging-wall anticline is slightly asymmetric, with a steeper forelimb than backlimb (Table 2). Footwall deformation, which is almost entirely viscous, produces a gentle footwall syncline beneath the ramp and causes uplift of the upper flat. As deformation proceeds, the upper ramp hinge translates towards the foreland relative to the lower ramp hinge, causing the ramp dip to decrease.

By following individual particles, stress paths in J space (Jamison 1993) and equivalent plastic and viscous strain histories can be tracked. Plastic strain accumulates only when the stress state is on the yield surface. Because we use a strain-hardening plastic material, the yield surface moves upward in J space as plastic strain accumulates, although only the initial yield surface is shown (Fig. 5). Viscous strain occurs for any non-zero value of $\sqrt{J_2'}$. A particle in the lower hanging wall (particle a; Fig. 5) undergoes viscous horizontal shortening over the lower flat. As the particle passes over the lower ramp hinge, its stress path contacts the yield surface and it undergoes plastic horizontal shortening. When the particle is above the ramp, the stress state falls below the yield surface because of increasing J_1 and decreasing $\sqrt{J_2'}$ and, thus, further plastic strain temporarily ceases. The incremental strain changes from horizontal shortening to extension approximately midway up the ramp. Over the upper ramp hinge, J_1 decreases and $\sqrt{J_2'}$ increases, and the stress state returns to the yield surface, resulting in additional plastic strain. This second phase of plastic deformation is horizontal exten-

sion, which is superposed on the earlier phase of horizontal shortening. As the particle moves over the upper flat, $\sqrt{J_2'}$ decreases and the stress state falls below the yield surface. Whereas the plastic deformation is distinctly episodic, viscous strain accumulates continuously but at varying rates. A particle in the upper hanging wall (particle b; Fig. 5) displays a similar deformational history, but the J-space stress path fluctuates less. The magnitudes of both plastic and viscous strain in the hanging wall decrease with distance from the fault, and a greater proportion of the total strain is viscous higher in the hanging wall.

In model B, with no viscous creep and the same plastic properties as viscous-plastic model A, the fold geometry (Fig. 6) is generally similar to model A. However, there is practically no footwall deformation in model B, and, consequently, the ramp shape remains relatively unchanged. J-space stress paths and strain histories in model B are also similar to model A (Fig. 7), although plastic strain and $\sqrt{J_2'}$ are consistently larger in model B.

Model C has viscous creep only (Fig. 8). In order to prevent separation along the fault surface, a lower viscosity was used in this model than in viscous-plastic model A. The use of this lower viscosity does not change the general form of the stress paths or strain histories. The hanging-wall anticline has a lower amplitude and is more rounded than the folds of the viscous-plastic or plastic models. The stress paths are relatively smooth because there is no constraining plastic yield surface (Fig. 9). In both the upper and lower hanging wall, the stress paths are loops in J space. J_1 reaches a maximum above the ramp, whereas $\sqrt{J_2'}$ reaches maxima above the lower and upper ramp hinges. Strain accumulates relatively smoothly with time in both the upper and lower hanging wall. Because of the considerable layer-parallel shortening of the footwall forward of the ramp, neither particle reaches the upper flat. After a displacement of 2.5 km, particles a and b are only above the upper ramp hinge.

Model D has the same hanging-wall material properties as viscous-plastic model A, but has a rigid footwall. This configuration eliminates shallowing and foreland translation of the ramp by footwall deformation, and allows the comparison of hanging-wall deformation above an undeformable vs a deformable footwall. The hanging-wall anticline of model D (Fig. 10) is flat-topped in the lower hanging wall, rounded at higher levels, and more open than model A. Magnitudes of equivalent plastic strain are similar in models A and D above the upper flat, but are higher in the backlimb of model D due to the maintenance of the steep ramp. The distributions of viscous strain in models A and D are nearly identical. Instead of the footwall uplift below the upper flat in model A, there is separation along the fault in the same positions in model D.

Layering and fault friction

The two-layer model E has a strong footwall and lower hanging wall, a weak upper hanging wall, and a
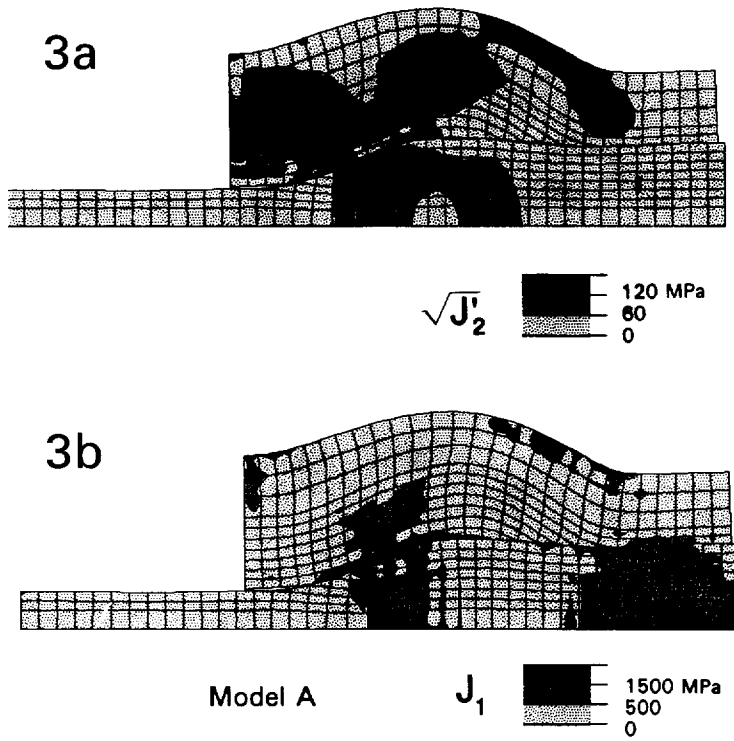
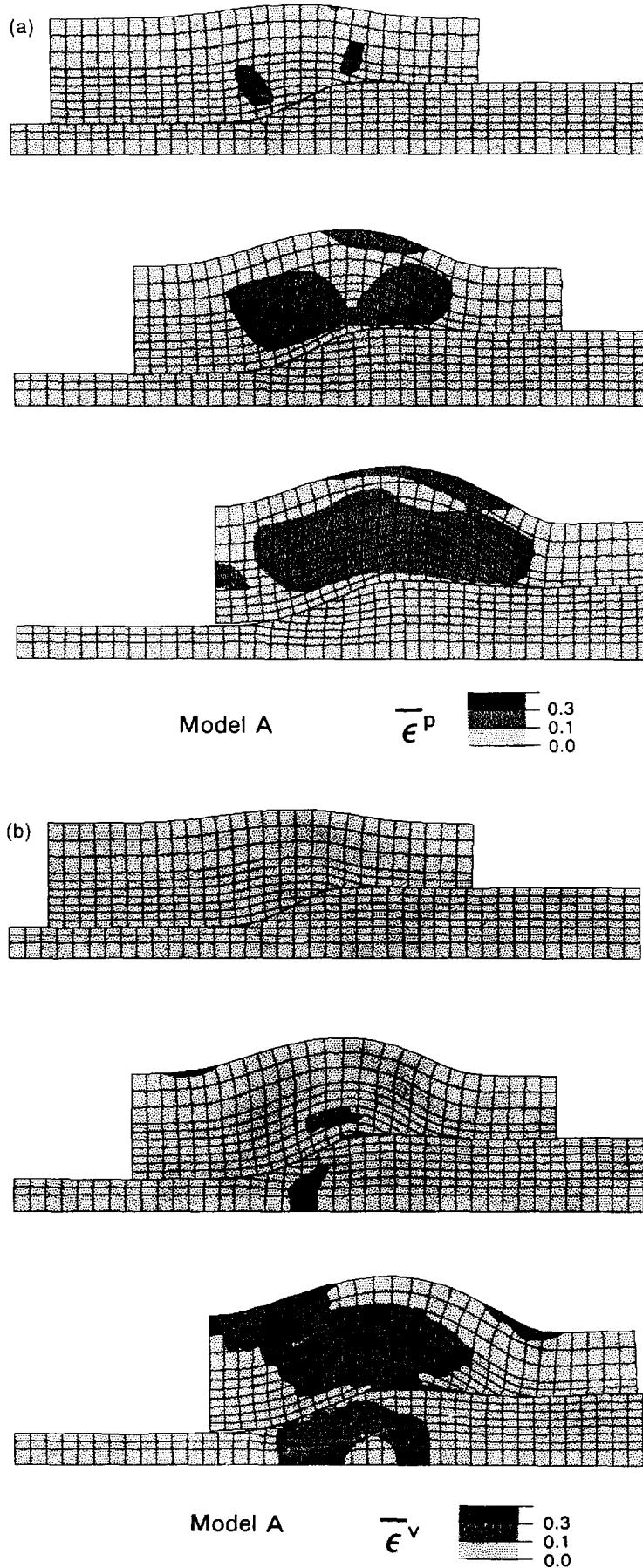Fig. 3. Contours of (a) $\sqrt{J_2'}$ and (b) J_1 at displacement 2.5 km for uniform viscous-plastic model A.

(a)

Model A $\overline{\epsilon}\,^{p}$ 0.3
                              0.1
                              0.0

(b)

Model A $\overline{\epsilon}\,^{v}$ 0.3
                              0.1
                              0.0

Fig. 4. Deformed grids and contours of (a) equivalent plastic strain and (b) equivalent viscous strain at displacements 0.5, 1.5 and 2.5 km for uniform viscous-plastic model A.

6

Model B $\overline{\epsilon}^{\,p}$ 0.3
0.1
0.0

8

Model C $\overline{\epsilon}^{\,v}$ 0.3
0.1
0.0

10

Model D $\overline{\epsilon}^{\,p}$ 0.3
0.1
0.0
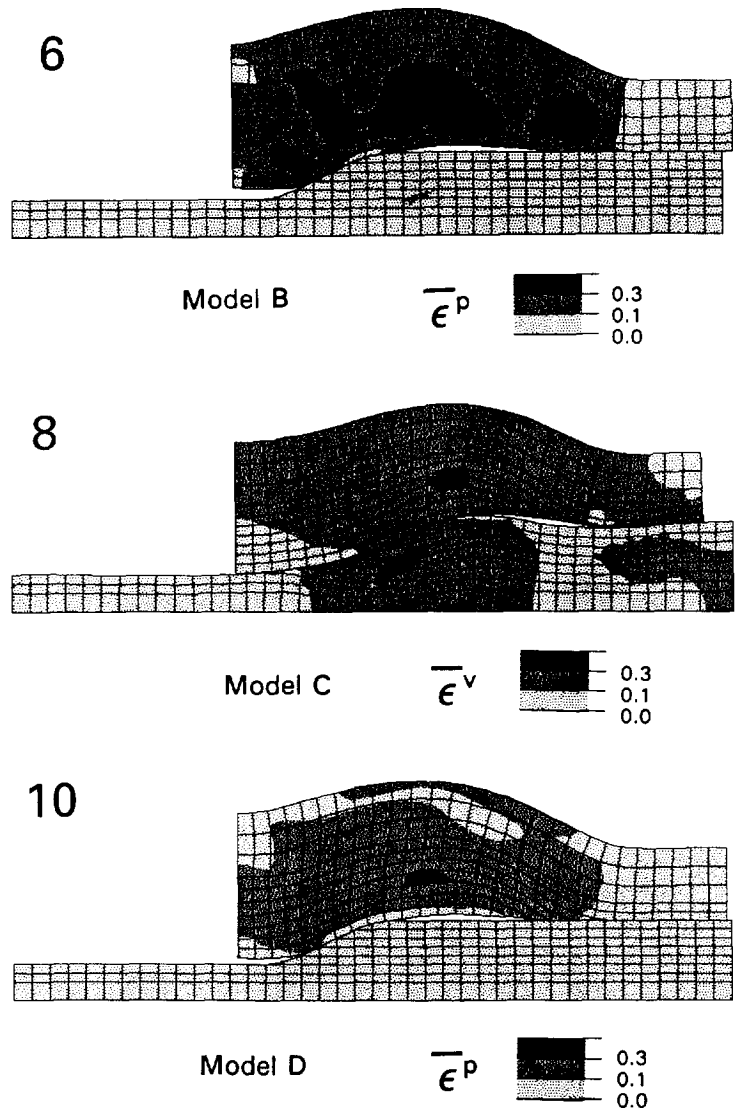
Fig. 6. Deformed grid and contours of equivalent plastic strain at displacement 2.5 km for plastic model B.

Fig. 8. Deformed grid and contours of equivalent viscous strain at displacement 2.5 km for viscous model C.

Fig. 10. Deformed grid and contours of equivalent plastic strain at displacement 2.5 km for model D, which has a viscous-plastic hanging wall and a rigid footwall.
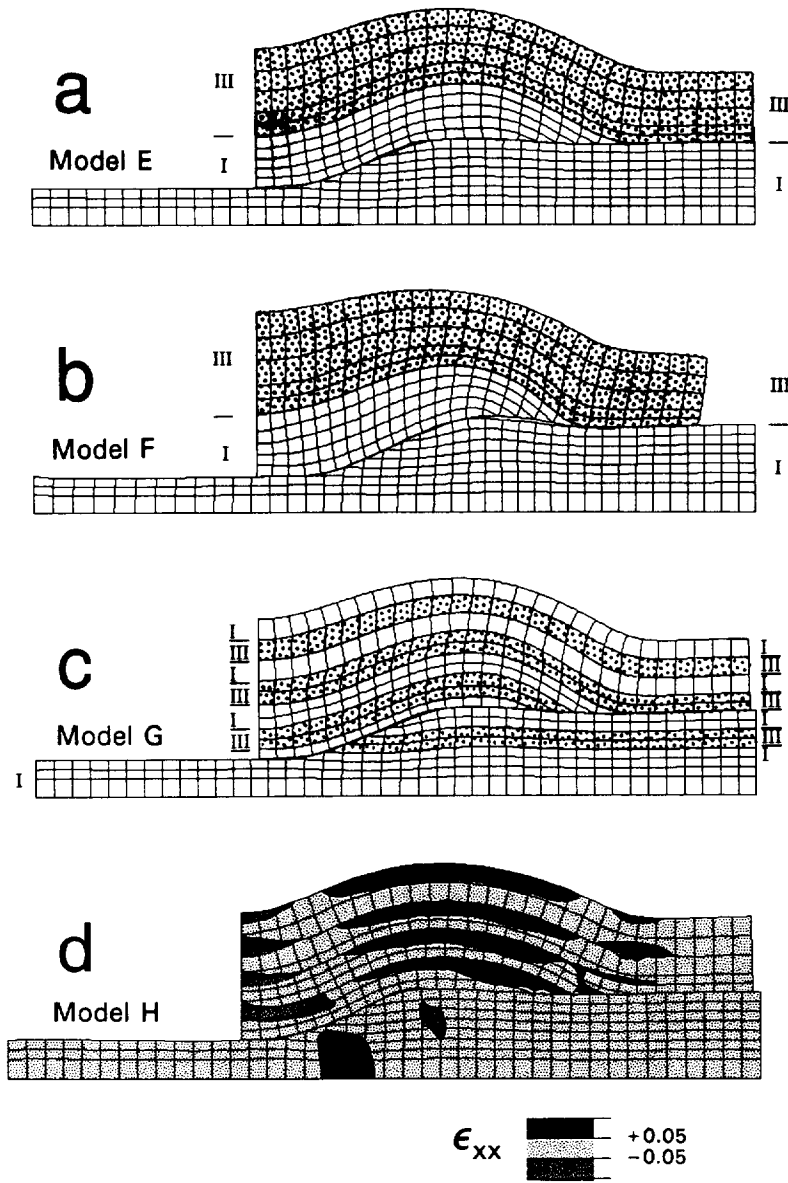
Fig. 11. Deformed grids at displacement 2.5 km for (a) two-layer model E with fault friction coefficient $\mu_F = 0.01$, (b) two-layer model F with $\mu_F = 0.3$, and (c) model G with six layers in the hanging wall. In (a)–(c), weaker layers composed of material III are stippled. (d) Model H with interlayer slip in the hanging wall. Contours are the horizontal component of strain ε_{xx} (extension is positive).
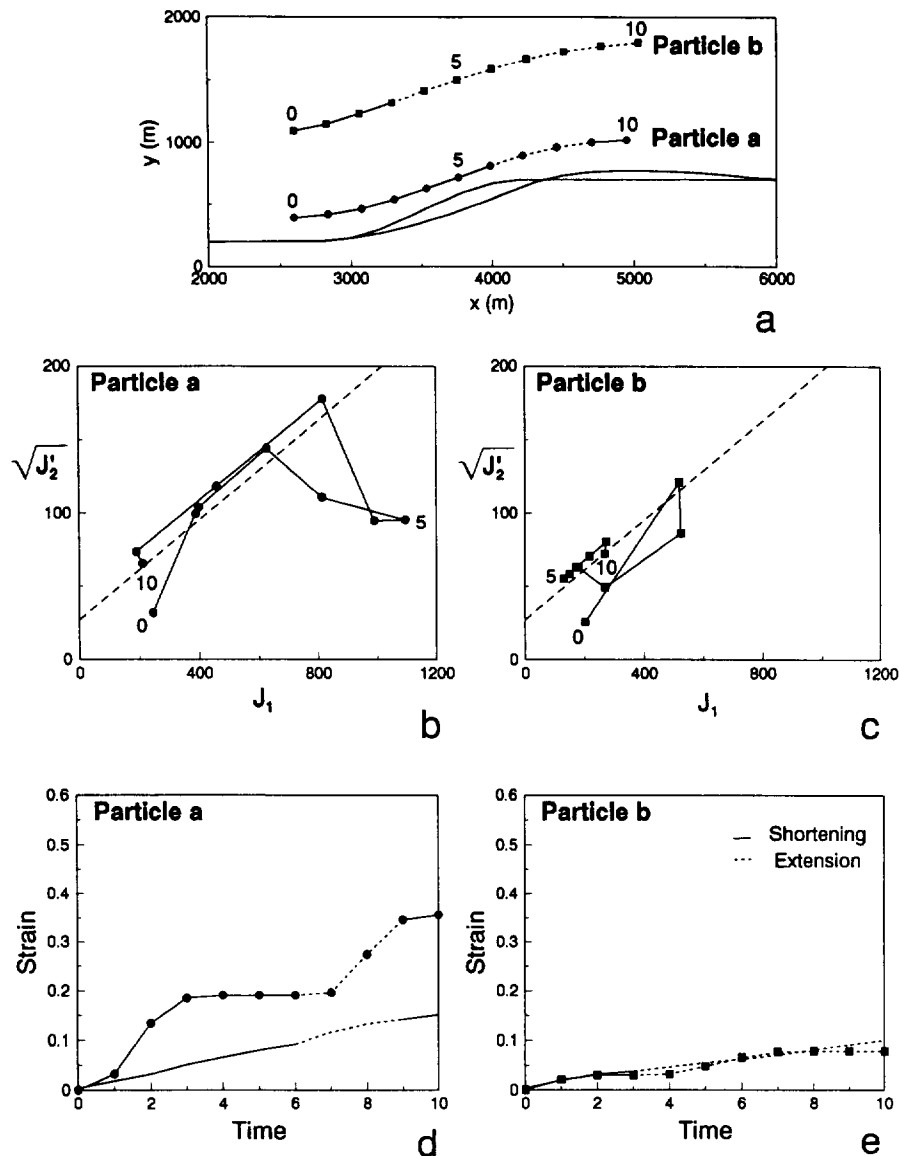
Fig. 5. (a) Displacement paths for two particles a and b in the uniform viscous-plastic model A. Each time increment represents 25,000 years (10 model time steps). Solid parts of curves represent times in which the horizontal component of incremental strain is shortening and dashed parts represent incremental strains of horizontal extension. (b) Stress path in $J_1 - \sqrt{J_2'}$ space for particle a. (c) Stress path for particle b. In (b) & (c), the dashed line is the initial plastic yield surface, and stresses are in MPa. (d) Equivalent plastic and viscous strains with time for particle a. (e) Equivalent plastic and viscous strains for particle b. In (d) & (e), curves with markers are equivalent plastic strain, curves without markers are equivalent viscous strain, and solid and dashed parts of curves are the same as in (a).

friction coefficient of 0.01 on the fault. Model F differs only by having a friction coefficient of 0.3 on the fault. No slip is allowed between the two layers in the hanging walls of these models. The deformed geometry of model E (Fig. 11a) is similar to the uniform model A. However, shear strain is concentrated at the base of the weak layer on the limbs of the hanging-wall anticline and there is more layer-parallel shortening of the upper hanging wall in the backlimb.

The hanging-wall anticline in model F (Fig. 11b) has more layer-parallel shortening in the backlimb and greater asymmetry (Table 2) than model E. In the lower hanging wall, this asymmetry is the result of a steeper forelimb. In the upper hanging wall, the forelimb has a dip that is similar to model E, but layer-parallel shortening causes the backlimb to have a shallower dip. The hanging wall above the upper flat is sheared, top to the

foreland, due to the fault drag, and there is a concentration of strain at the base of the weak layer in the hinge of the leading syncline. There is more footwall deformation in model F than in model E, manifested as layer-parallel shortening beneath the ramp and layer-parallel extension beneath the lower flat.

Multilayer model G has six alternating strong and weak layers, each 200 m thick. No slip is allowed between these layers. The gross fold geometry of model G is similar to that of single-layer model A. Strain is concentrated in the weak layers (Fig. 11c), and the sense of shear on the limbs of the hanging-wall anticline is consistent with flexural-flow folding. As in model A, plastic strain accumulates as material passes over the ramp hinges. The final equivalent plastic strain distribution consists of bands of high strain in the weak layers. $\sqrt{J_2'}$ and J_1 are highest in the strong layers. Top to the
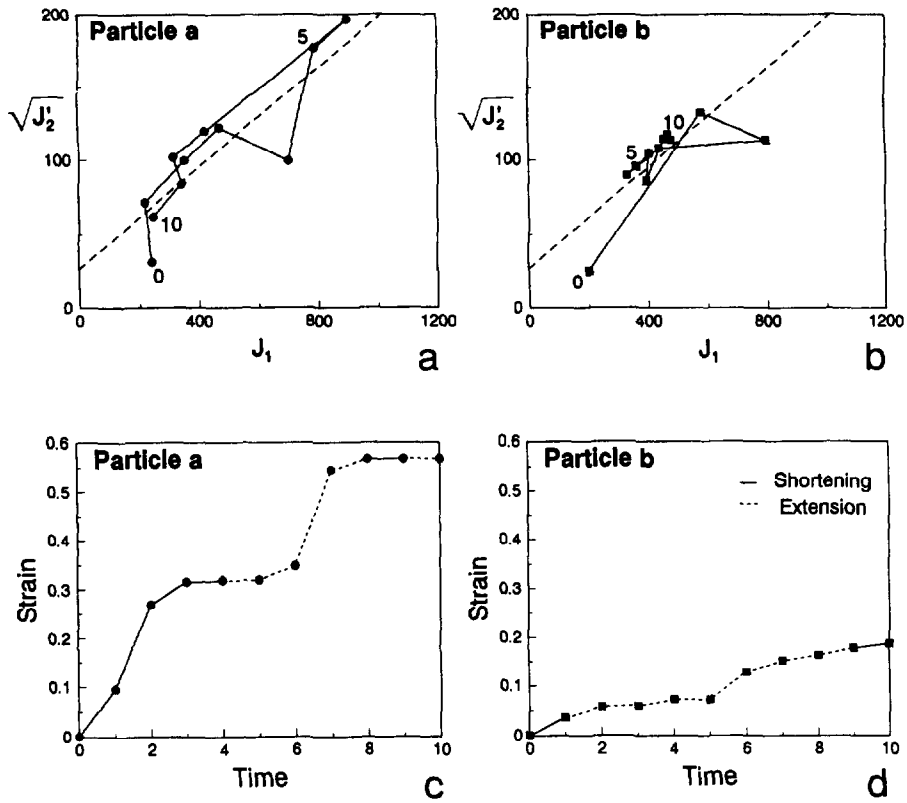
Fig. 7. Stress paths in $J_1 - \sqrt{J_2'}$ space for (a) particle a and (b) particle b (same initial coordinates as in Fig. 5) in the plastic model B. Equivalent plastic strain with time for (c) particle a and (d) particle b.
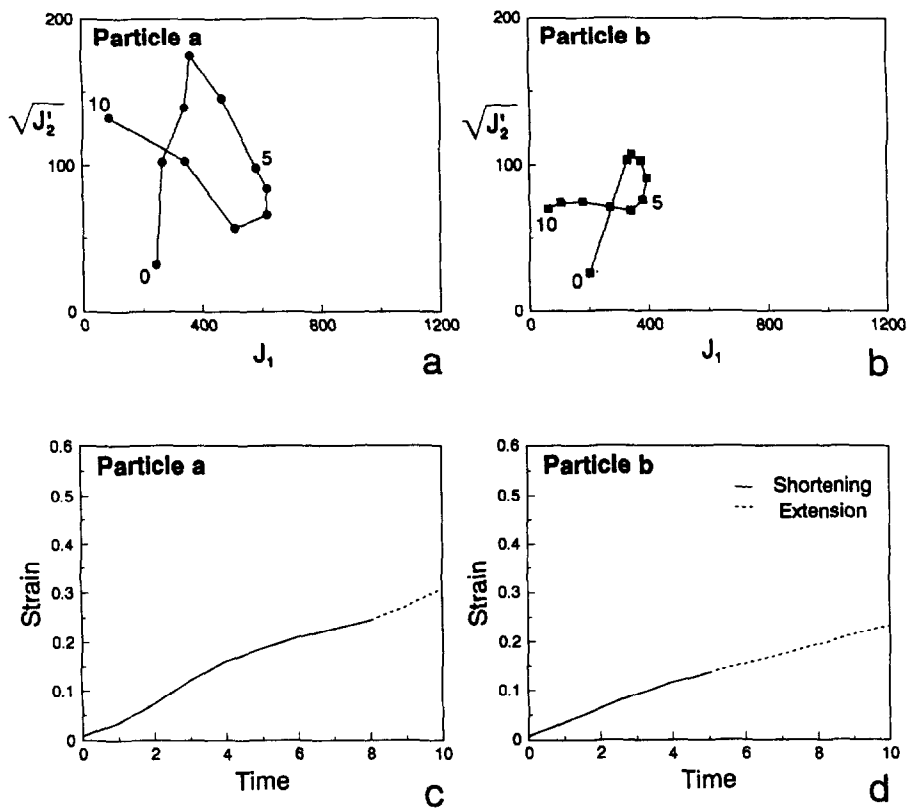

Fig. 9. Stress paths in $J_1 - \sqrt{J_2'}$ space for (a) particle a and (b) particle b (same initial coordinates as in Fig. 5) in the viscous model C. Equivalent viscous strain with time for (c) particle a and (d) particle b.

foreland shear strain develops immediately beneath the ramp, and is concentrated in the weak layer.

Interlayer slip

Model H allows interlayer slip along three frictional surfaces within the hanging wall. The material properties of the footwall and all the hanging-wall layers are the same as those in model A. The hanging-wall slip surfaces are spaced 300 m apart, and the slip surfaces and the fault all have μ_F = 0.01. Where each interlayer slip surface intersects the edges of the model, it is pinned across the interface. Interlayer slip is concentrated on the limbs of the hanging-wall anticline, with shear senses consistent with flexural-slip folding (Fig. 11d). Layer thicknesses remain nearly constant through the fold. Most of the displacement on the slip surfaces accumulates as they move over the ramp hinges. These surfaces slip top to the foreland over the lower ramp hinge, and top to the hinterland over the upper ramp hinge. On the lowest interlayer slip surface, which truncates against the fault, the slip is greater on the backlimb (maximum of ~200 m) than on the forelimb. On the two higher slip surfaces, the maximum interlayer slips on the forelimb and backlimb are nearly equal. Relative to model A, the hanging-wall anticline has a lower amplitude and is more symmetric (Table 2). The anticline has a flat top in the lower hanging wall and becomes more rounded in the upper hanging wall.

The slip surfaces divide the hanging wall into discrete layers, each of which develops a neutral surface. Layer-parallel extension develops in bands around the outer arcs of the hanging-wall anticline and, to a lesser extent, in the outer arcs of the leading and trailing synclines. Layer-parallel shortening develops in the inner arcs of hanging-wall folds, with higher magnitudes of shortening in the leading and trailing synclines than in the anticline. J_1 is highest in the inner arcs of the trailing syncline and hanging-wall anticline, and $\sqrt{J_2'}$ is high in fold hinges and above the ramp hinges.

DISCUSSION

The finite-element models simulate both fold geometry and the distribution and timing of deformation in fault-bend folds. The fold geometries of the models can be compared with those of geometric models of fault-bend folds, which relate fold geometry to fault configuration (e.g. Suppe 1983, Jamison 1987). Although the geometric models generally use a kinked-hinge fold geometry, the angular relationships for a mode I fault-bend fold are fundamentally the same if the hinges are curved (Jamison 1987 and unpublished data). In the geometric models, the backlimb dip δ_b (Fig. 1) of a fault-bend fold is equal to the ramp dip. In the finite-element models, the ramp dip is initially 26.5°, but decreases by a few degrees during the model evolution. The final maximum backlimb dips range from 19° to 26° (Table 2). The smallest backlimb dip occurs in the plastic
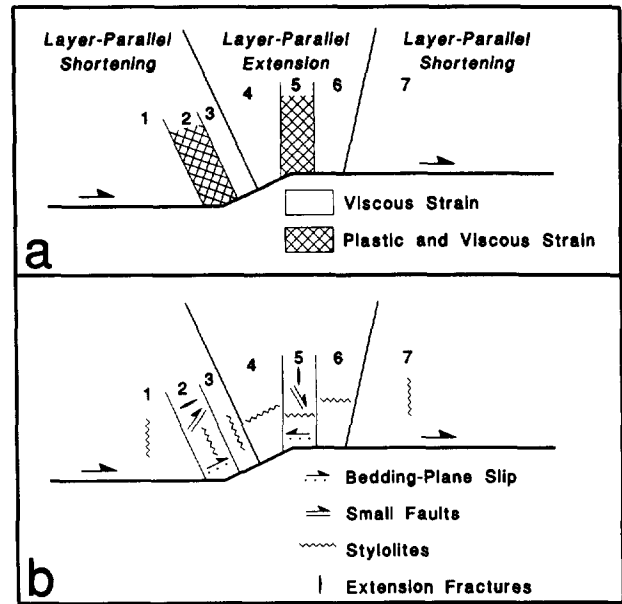

Fig. 12. Schematic drawing of (a) regions of viscous and plastic strain and layer-parallel shortening and extension in the models, and (b) the possible sequence of deformation mechanisms.

model B, in which there is substantial separation along the fault (Fig. 6). The forelimb dip δ_f of a kinked-hinge geometric model with a 26.5° ramp dip and constant bed thickness is 36° (Suppe 1983). In the geometric models, the forelimb dip depends only on the initial ramp geometry, and would not be affected by later shallowing of the ramp. Maximum forelimb dips in the finite-element models range from 29° to 39° (Table 2). Model C (Fig. 8), with low hanging-wall strength, and model F (Fig. 11b), with high fault friction, have the steepest forelimb dips. In addition, layer thicknesses are not constant in the hanging-wall anticlines of the finite-element models. For example, in model A (Fig. 3), there is ~20% layer thickening in the hinge and ~5% thinning in the forelimb. According to the geometric models, layer thickening in the hinge should increase the forelimb dip (Jamison, unpublished data), whereas thinning in the forelimb should decrease the forelimb dip (Jamison 1987). The forelimb dip of model H (Fig. 11d), with interlayer slip surfaces in the hanging wall, matches the geometric models more poorly than the forelimb dips of models without interlayer slip surfaces (Table 2), despite the relatively constant layer thicknesses in this model. In general, the limb dips of the geometric models are similar to those in the finite-element models, although fold geometries in the finite-element models are functions of material properties and fault friction in addition to ramp dip.

If pressure-dependent plastic deformation simulates cataclasis and viscous deformation simulates pressure solution creep, then the results of our models can be used to infer a sequence of deformation mechanisms. The models without slip surfaces in the hanging wall simulate the following sequence of deformation for a particle moving over a ramp (Fig. 12a); (1) viscous shortening, (2) plastic and viscous shortening, (3) viscous shortening, (4) viscous extension, (5) plastic and

viscous extension, (6) viscous extension, and (7) viscous shortening. From these results, we infer the following sequence of deformation mechanisms (Fig. 12b): (1) transport-perpendicular stylolites, (2) mesoscopic thrust faults, transport-parallel extension fractures, and top to the foreland bedding-plane slip, (3) transport-perpendicular stylolites, (4) bedding-parallel stylolites, (5) mesoscopic normal faults, transport-perpendicular extension fractures, and top to the hinterland bedding-plane slip, (6) bedding-parallel stylolites, (7) transport-perpendicular stylolites. Kilsdonk & Wiltschko (1988), in a study of the ramp region of the Pine Mountain fault, recognized an early deformational phase characterized by mesoscopic thrust faults, transport-parallel extension fractures, and transport-perpendicular stylolites, which may correlate with our stages 1–3. They also observe a later phase characterized by mesoscopic normal faults and transport-perpendicular extension fractures, which may correlate with our stage 5. Wiltschko et al. (1985) recognized early transport-perpendicular stylolites, which may correlate with our stage 1, and later transport-perpendicular extension fractures, mesoscopic faults and bedding-plane slip, which may correlate with our stages 2 and 5. Thus, our model results are consistent with field observations, although the complete suite of deformational stages indicated by these models has not been recognized in the observational studies.

In models without slip surfaces in the hanging wall, a particle moving over the ramp experiences shortening over the lower ramp hinge followed by extension over the upper ramp hinge and then by further shortening. This deformation history agrees with linear viscous flow models (Kilsdonk & Fletcher 1989). Superposed on the shortening and extension above ramp hinges is neutral-surface bending of the hanging wall, characterized by extension in outer arcs and shortening in inner arcs of folds. With the material properties used here, this neutral-surface bending is relatively minor in models without interlayer slip. Our models indicate the importance of layering and interlayer slip in determining the style of deformation, in agreement with previous studies of deformation at ramps (Serra 1977, Spang et al. 1981, Wiltschko 1981, Chester et al. 1991). The hanging-wall anticline is more symmetric and has a lower amplitude if the hanging wall contains interlayer slip surfaces. Strain in multilayer models is concentrated in the weak layers or taken up on discrete interlayer slip surfaces, especially in the accommodation of shear strain on the limbs of the hanging-wall anticline. Unlike models with a pervasive anisotropy (Wiltschko 1981), layers between discrete slip surfaces undergo significant neutral-surface bending in our models. Thus, if interlayer slip is important, the deformation sequence proposed above may be altered by small scale neutral-surface bending. The magnitude of frictional resistance along the fault, relative to hanging-wall and footwall strengths, also influences the fold geometry and strain in the hanging wall, in agreement with experimental rock models (Morse 1977, Chester et al. 1991) and linear viscous models (Berger &

Johnson 1980). Higher frictional resistance leads to greater fold asymmetry, more layer-parallel shortening in the backlimb of the hanging-wall anticline, and more footwall deformation.

In models that allow footwall deformation, movement of the hanging wall over the ramp produces significant deformation beneath the ramp. Interlayer slip in the hanging wall and low fault friction reduce this footwall deformation. Our models indicate that, in a viscous-plastic material, footwall deformation is dominated by the viscous component because of the high J_1 beneath the ramp. This viscous deformation represents pressure solution creep in natural rock deformation. Although pressure solution creep has been recognized as a mechanism of footwall deformation beneath natural ramps (Protzman & Mitra 1990, Evans & Neves 1992), there are no data on its importance relative to other mechanisms. Early layer-parallel shortening by pressure solution in thrust belts (e.g. Wiltschko et al. 1985) could be a result of this footwall deformation. In our models, the boundary condition of no vertical displacement on the base simulates a rigid basement and suppresses the development of a major footwall syncline, compared to the infinite half-space footwall in the model of Kilsdonk & Fletcher (1989), in which the footwall syncline has a shape similar to that of the hanging-wall anticline. In our models, variations in the amount and style of footwall deformation do not have a large effect on hanging-wall deformation.

CONCLUSIONS

We have used finite-element models with viscous and plastic material properties to simulate pressure solution creep and cataclasis, respectively, during the development of fault-bend folds. The relative activity of these competing processes is determined by the magnitude of the stress invariants J_1 and $\sqrt{J_2'}$. In the models, $\sqrt{J_2'}$ is highest above ramp hinges and below the ramp, whereas J_1 is highest above and below the ramp. Plastic strain accumulates primarily above the ramp hinges. Viscous strain is more widely distributed and accumulates continuously but at varying rates. Viscous deformation dominates above the ramp and flats, where plastic deformation is negligible. Because of the high J_1 below the ramp, footwall deformation is predominantly viscous. The accumulation of plastic strain in material as it moves over ramp hinges creates a band of high equivalent plastic strain in the lower hanging wall. Hanging-wall material undergoes layer-parallel shortening on the lower flat and lower part of the ramp, extension on the upper part of the ramp and upper flat, and shortening on the upper flat. These changes in the dominance of plastic and viscous strain and layer-parallel shortening and extension during movement over a model ramp indicate a complex but predictable sequence of deformation mechanisms in natural fault-bend folds. In multilayer models, strain concentrates in the weak layers, especially on the limbs of the hanging-wall anticline. In

models with slip surfaces in the hanging wall, the shear strain on fold limbs is accommodated by interlayer slip, and layers between slip surfaces develop individual neutral surfaces. The sense of slip on these surfaces changes from top to the foreland over the lower ramp hinge to top to the hinterland over the upper ramp hinge.

REFERENCES

Apperson, K. D. 1993. Structural controls on early layer parallel shortening. *Eos* 74, 301.

Apperson, K. D. & Goff, D. F. 1991. Deformation of thrust ramps and footwalls observed in numerical models. *Eos* 72, 514–515.

Berger, P. & Johnson, A. M. 1980. First-order analysis of deformation of a thrust sheet moving over a ramp. *Tectonophysics* 70, T9–T24.

Chester, J. S., Logan, J. M. & Spang, J. H. 1991. Influence of layering and boundary conditions on fault-bend and fault-propagation folding. *Bull. geol. Soc. Am.* 103, 1059–1072.

Drucker, D. C. & Prager, W. 1952. Soil mechanics and plastic analysis or limit design. *Q. Appl. Math.* 10, 157–165.

Evans, J. P. & Neves, D. S. 1992. Footwall deformation along Willard thrust, Sevier orogenic belt: implications for mechanisms, timing and kinematics. *Bull. geol. Soc. Am.* 104, 516–527.

Fischer, M. W. & Coward, M. P. 1982. Strains and folds within thrust sheets: an analysis of the Heilam sheet, northwest Scotland. *Tectonophysics* 88, 291–312.

Fletcher, R. C. 1987. Anisotropic plastic solid as a model for layered sedimentary rock at yield and the internal structures of fold-and-thrust belts. *Geol. Soc. Am. Abs. w. Prog.* 19, 664.

Groshong, R. H. 1988. Low-temperature deformation mechanisms and their interpretation. *Bull. geol. Soc. Am.* 100, 1329–1360.

Hill, R. 1950. *The Mathematical Theory of Plasticity*. Oxford University Press, Oxford.

Jaeger, J. C. & Cook, N. G. W. 1971. *Fundamentals of Rock Mechanics*. Chapman & Hall, London.

Jamison, W. R. 1987. Geometric analysis of fold development in overthrust terrains. *J. Struct. Geol.* 9, 207–219.

Jamison, W. R. 1993. Stress spaces and stress paths. *J. Struct. Geol.* 14, 1111–1120.

Johnson, A. M. 1971. *Physical Processes in Geology*. Freeman, Cooper and Co., San Francisco.

Johnson, A. M. & Berger, P. 1989. Kinematics of fault-bend folding. *Eng. Geol.* 27, 181–200.

Kilsdonk, B. & Fletcher, R. C. 1989. An analytical model of hanging-wall and footwall deformation at ramps on normal and thrust faults. *Tectonophysics* 163, 153–168.

Kilsdonk, B. & Wiltschko, D. V. 1988. Deformation mechanisms in the southeastern ramp region of the Pine Mountain block, Tennessee. *Bull. geol. Soc. Am.* 100, 653–664.

McClay, K. R. 1992. Glossary of thrust tectonics terms. In: *Thrust Tectonics* (edited by McClay, K. R.). Chapman & Hall, London, 419–433.

Morse, J. D. 1977. Deformation in the ramp regions of overthrust faults—Experiments with small-scale rock models. *Wyoming Geol. Assoc. Guidebook, 29th Ann. Field Conf.* 457–470.

Paterson, M. S. 1978. *Rock Deformation—The Brittle Field*. Springer-Verlag, Berlin.

Protzman, G. M. & Mitra, G. 1990. Strain fabric associated with the Meade thrust sheet: implications for cross-section balancing. *J. Struct. Geol.* 12, 403–417.

Rich, J. L. 1934. Mechanics of low-angle overthrust faulting illustrated by the Cumberland thrust block, Virginia, Kentucky and Tennessee. *Bull. Am. Ass. Petrol. Geol.* 18, 1584–1596.

Rudnicki, J. W. & Rice, J. R. 1975. Conditions for the localization of deformation in pressure-sensitive dilatant materials. *J. Mech. Phys. Solids* 23, 371–394.

Rutter, E. H. 1976. The kinetics of rock deformation by pressure solution. *Phil. Trans. R. Soc. Lond.* 283, 203–219.

Sanderson, D. J. 1982. Models of strain variation in nappes and thrust sheets: a review. *Tectonophysics* 88, 201–233.

Serra, S. 1977. Styles of deformation in the ramp regions of overthrust faults. *Wyoming Geol. Ass. Guidebook, 29th Ann. Field Conf.* 487–498.

Spang, J. H., Walcott, T. L. & Serra, S. 1981. Strain in the ramp regions of two minor thrusts, southern Canadian Rocky Mountains. In: *Mechanical Behavior of Crustal Rocks: The Handin Volume* (edited by Carter, N. L., Friedman, M., Logan, J. M. & Stearns, D. W.). *Am. Geophys. Un. Monogr.* 24, 243–250.

Suppe, J. 1983. Geometry and kinematics of fault-bend folding. *Am. J. Sci.* 283, 684–721.

Turcotte, D. L. & Schubert, G. 1982. *Geodynamics: Applications of Continuum Physics to Geological Problems*. John Wiley and Sons, New York.

Wiltschko, D. V. 1979. A mechanical model for thrust sheet deformation at a ramp. *J. geophys. Res.* 84, 1091–1104.

Wiltschko, D. V. 1981. Thrust sheet deformation at a ramp: Summary and extensions of an earlier model. In: *Thrust and Nappe Tectonics* (edited by McClay, K. R. & Price, N. J.). *Spec. Publ. geol. Soc. Lond.* 9, 55–63.

Wiltschko D. V. & Dorr, J. A. 1983. Timing and deformation in overthrust belt and foreland of Idaho, Wyoming, and Utah. *Bull. Am. Ass. Petrol. Geol.* 67, 1304–1322.

Wiltschko, D. V., Medwedeff, D. A. & Millson, H. E. 1985. Distribution and mechanisms of strain within rocks on the northwest ramp of Pine Mountain block, southern Appalachian foreland: a field test of theory. *Bull. geol. Soc. Am.* 96, 426–435.